Supplementary Information of "Modulation of the electrocatalytic performance of rGO/CoCuFe[Ni(CN)$_4$] pillared with pyridine derivatives in Zinc-air batteries."

E. Arturo Quintanilla-Serrano[a*], Próspero Acevedo-Peña[b]*, Marlene González[a], and Edilso Reguera[a]*

[a] *Instituto Politécnico Nacional, Laboratorio Nacional de Conversión y Almacenamiento de Energía, CICATA-Legaria, 11500. Mexico City, Mexico.*

[b] *SECIHTI-Instituto Politécnico Nacional, Laboratorio Nacional de Conversión y Almacenamiento de Energía, CICATA-Legaria, 11500. Mexico City, Mexico.*

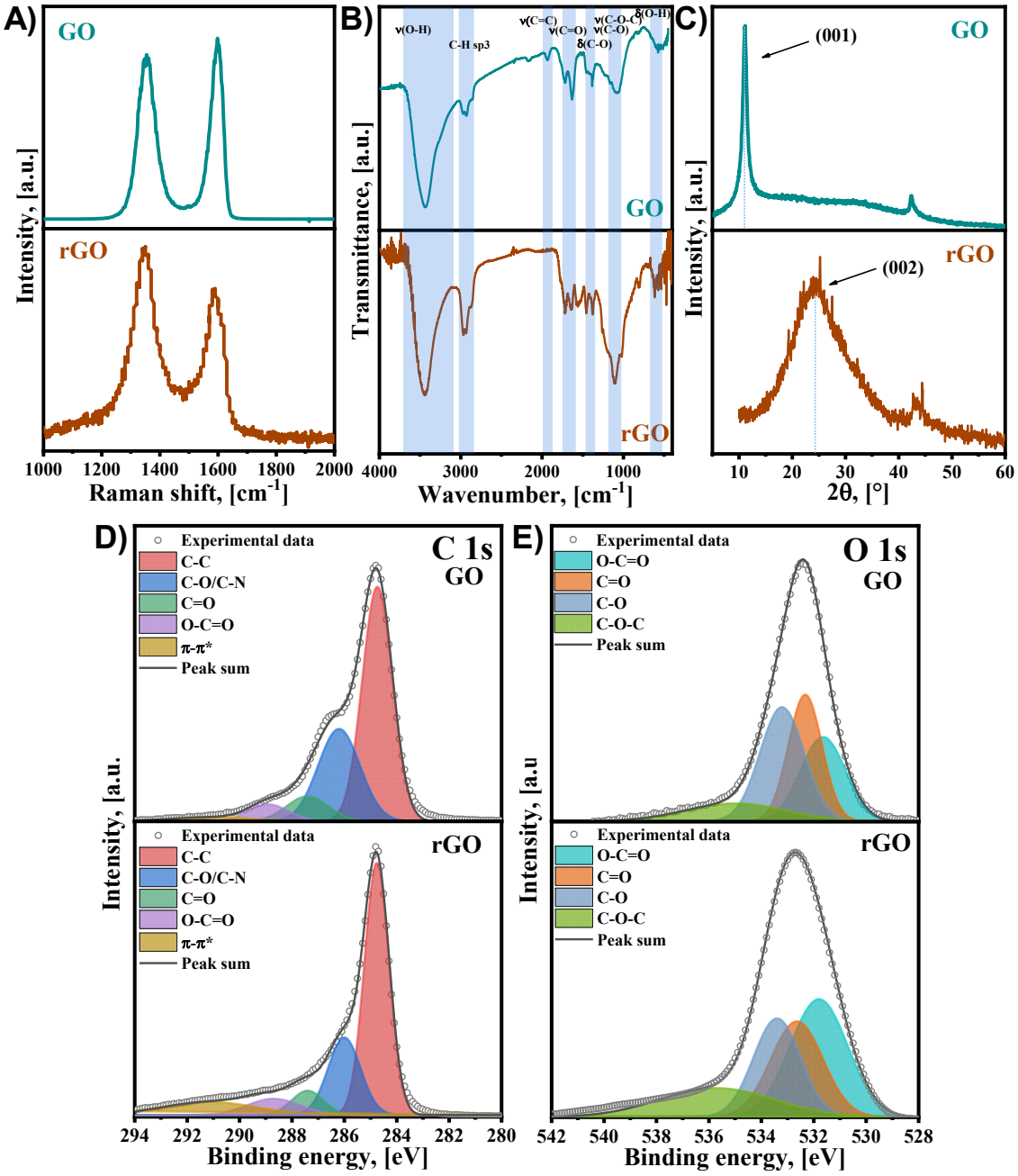

Fig. S1. (A) XRD patterns, (B) Raman spectra, (C) FTIR spectra. High-resolution XPS spectra in (D) C 1s region and (E) O 1s region of GO and rGO.

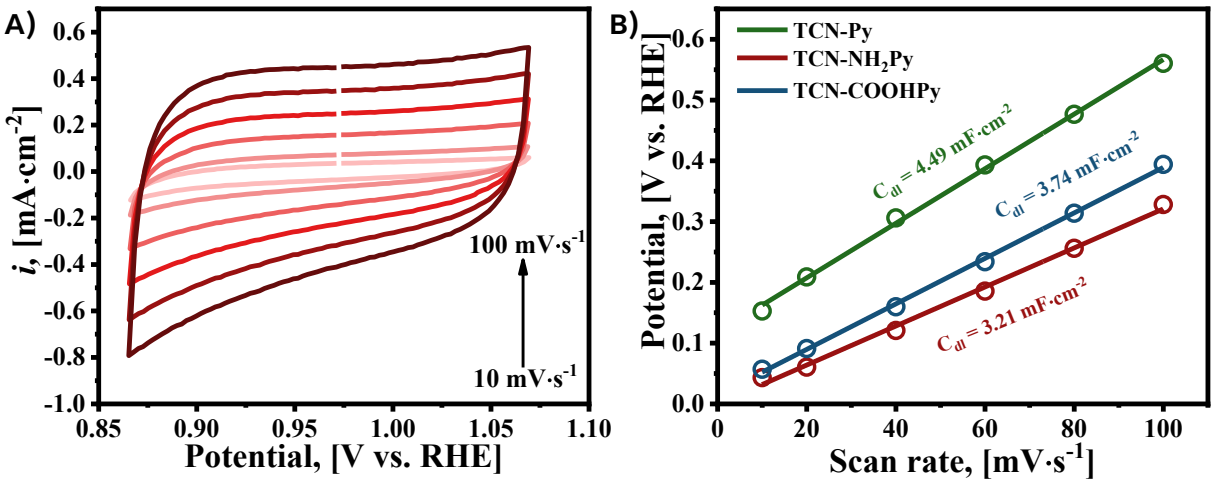

Figure S2. (A) Cyclic voltammetry curves in a potential window where no Faradaic processes occur at various scan rates (10, 20, 40, 60, 80, and 100 mVs^{-1}) to calculate ECSA of TCN-NH_2Py, and (B) Current density vs Scan rate plot for TCN-Py, TCN-NH_2Py, and TCN-COOHPy.

After obtaining the C_{dl} (double layer capacitance), the next expression is applied to finally, calculate the ECSA:

$$ECSA = \frac{C_{dl}}{C_s}$$

Where C_s is the specific capacitance reported for carbon-based materials and is taken as a default value (C_s=*40 μF*).

To calculate V vs. RHE from V vs. Hg/HgO, the next expression can be used:

$$\boldsymbol{E_{V\ vs.RHE}} = E_{V\ vs.Hg/HgO} + (0.059\,pH) + 0.140$$

Table S1. The OER and ORR performance of several MOFs and MOF-derived materials documented in the literature is compared to the values obtained in this study.

Material	**On-set potential (OER), [V vs. RHE]**	**Overpotential @10 mA cm^{-2} [mV vs. RHE] (OER)**	**Tafel slope [mV dec^{-1}] (OER)**	**On-set potential (ORR), [V vs. RHE]**	**Overpotential @1 mA cm^{-2} [mV vs. RHE] (ORR)**	**Half-wave potential [V vs. RHE]/Tafel slope [mV dec^{-1}]**	**Ref.**
TCN-Py (this work)	1.58	423	73	~0.82	413	-/72	
TCN-NH_2Py (this work)	1.55	402	82	~0.82	418	-/81	
TCN-COOHPy (this work)	1.56	380	41	~0.82	419	-/67	
CoTCN	~1.61	430	41.9	0.74	569	-/147	[1]
CoTCN:rGO (3:1)	1.6	390	61.84	~0.83	426	-/75	[1]
CoTCN:rGO (1:1)	~1.61	430	62.56	~0.83	412	-/80	[1]
CoTCN:rGO (1:3)	1.63	460	75.53	~0.83	401	-/82	[1]
rGO	1.65	360	244.4	~0.83	404	-/70	[1]
NiPc–MOF	1.48	250	74	-	-	-	[2]
Ni-MOF	-	406	58.5	-	-	-	[3]
V-Ni-MOF/NF	-	259	67.5	-	-	-	[4]

Co-MOF/CP	-	318	132.5	-	-	-	[5]
NiFe-based MOF	-	310	47.4	-	-	-	[6]
Co–Fe-MOF 2:1	-	310	53	-	-	-	[7]
Co-MOF@Fe-MOF	-	290	40.9	-	-	-	[8]
M-NC*	-	-	-	0.963	353	-/<60	[9]
Zn-MOF*	-	-	-	0.384	700	-/70	[10]
Co-MOF*	-	-	-	0.91	-	0.82/-	[11]
Cu(phen-NO3) (BTC)*	-	-	-	0.998	-	0.805/-	[12]
PB*	-	-	-	0.95	-	0.82/-	[13]
MOF-253*	-	-	-	0.98	-	0.84/-	[14]
Fe/IRMOF-3*	-	-	-	1.02	-	0.88/-	[15]

**heat treated MOF*

Table S2. The performance of various metal-organic frameworks (MOFs) and MOF-derived materials utilized in zinc-air batteries reported in the literature compared with the values obtained in this study.

Material	ΔE [V]	Power density, [mW cm^{-2}]	Specific capacity, [mA h g^{-1}]	Ref.
TCN-NH_2Py (this work)	0.87 V @ 5 mA cm^{-2}	-	795	
CoTCN:rGO(1:1)	0.96 V @ 5 mA cm^{-2}	-	760	[1]
Co_{SAs}@NC920*	0.858 V @ 2 mA cm^{-2}	166	847.5	[16]
FeCo-NC*	-	146.8	855.74	[17]
CC@FeCoNiMoRu-HEA/C + Pt/C*	0.858 V @ 5 mA cm^{-2}	171.5	795.9	[18]
NiFe-MOF/$NiFe_2O_4$*	0.88 V @ 2 mA cm^{-2}	158.4	700	[19]
CoFe@NCNT/NCS-800 **	0.79 V @ 5 mA cm^{-2}	196.1	827.21	[20]
S-FeNi/NiFe2O4@NC-800 **	0.76 @ 10 mA cm^{-2}	129	837	[21]
FeNi@NC-900 *	0.72 V @ 10 mA cm^{-2}	119	830.1	[22]

**heat treated MOF, **Hofmann-type MOF-derived and heat treated.*

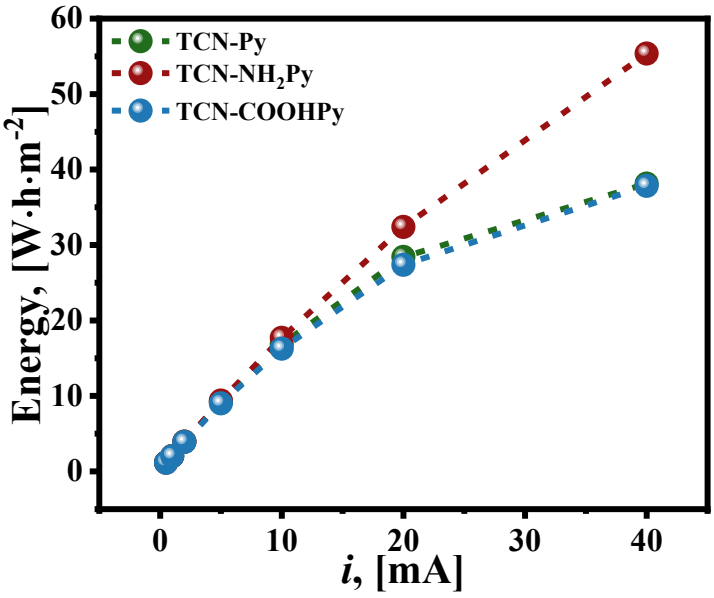

Figure S3. Energy dependence of current derived from the discharge test of every composite assembled in Zn-Aire batteries.

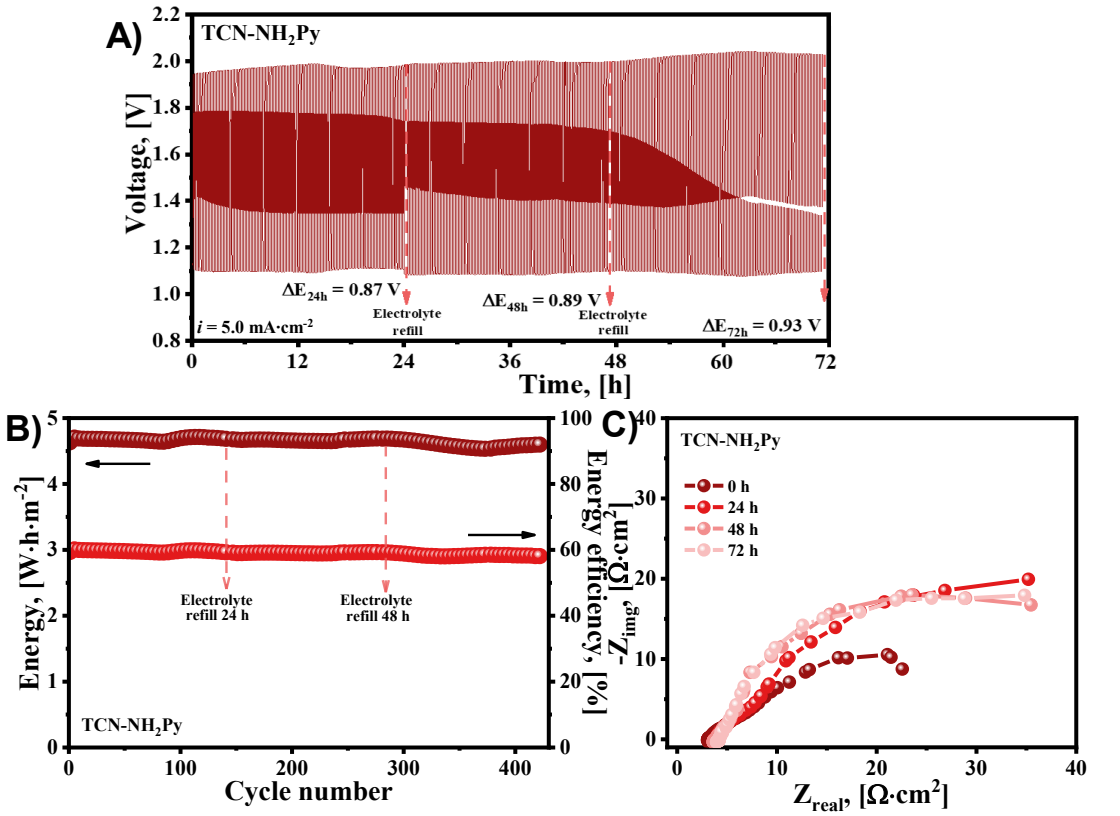

Figure S4. (A) Galvanostatic charge-discharge cycling performance at 5.0 mA·cm^{-2}, (B) Energy and energy efficiency, C) Nyquist plot at 0, 24, 48, and 72 h of Zn-Air battery cycling performance at -1.0 mA·cm^{-2}.

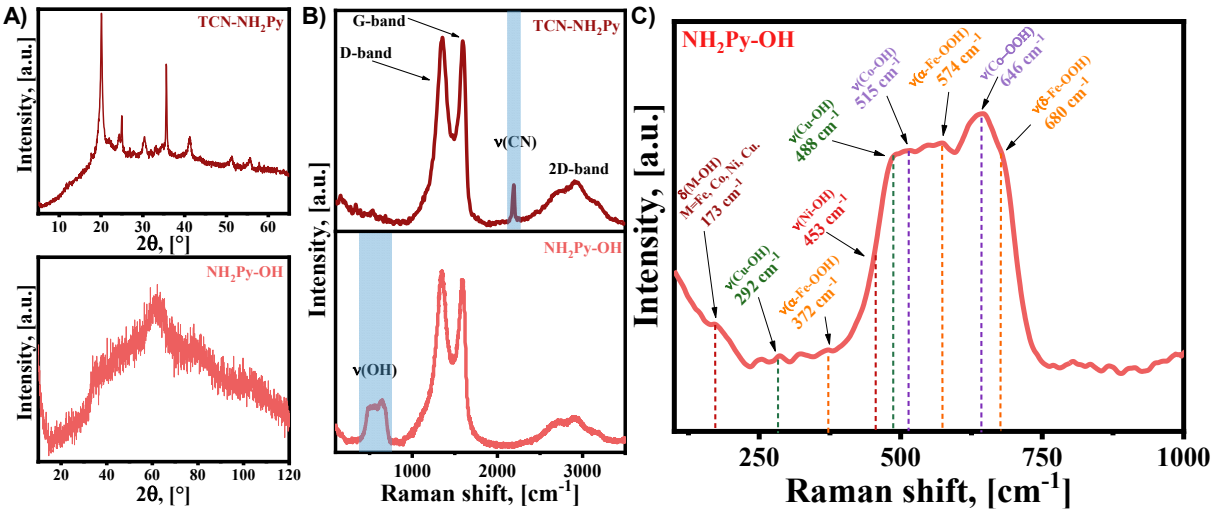

Figure S5. (A) XRD patterns and (B) Raman spectra for TCN-NH$_2$Py fresh and cycled (NH$_2$Py-OH), and C) Raman spectra adjusted for NH$_2$Py-OH.

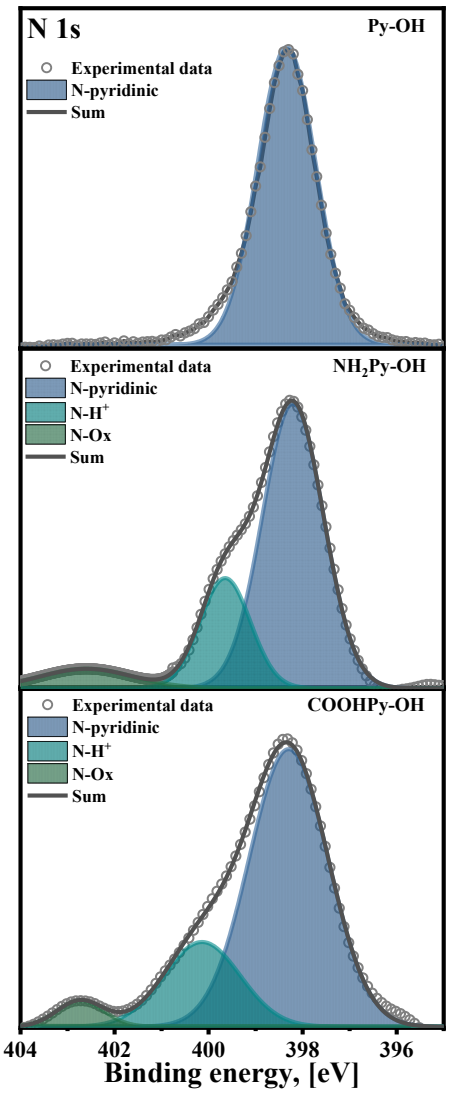

Figure S6. High-resolution N 1s XPS spectrum of the cycled electrodes.

Table S3. BET surface area, total pore volume, and average pore width of Py-OH, NH_2Py-OH, and COOHPy-OH obtained from N_2 adsorption-desorption isotherms.

Sample	BET surface area (m^2/g)	Total pore volume (cm^3/g)	Average pore width (Å)
Py-OH	51.35	0.1288	100.4
NH_2Py-OH	83.34	0.2683	128.8
COOHPy-OH	48.04	0.1185	98.7

DC and AC magnetic measurements support information.

A convenient method for classifying the freezing/blocking processes obtained by the dynamic measurements is determined by the Mydosh parameter Φ, which is an empirical parameter that denotes the relative shift of the temperature per frequency decade [23]:

$$\Phi = \frac{\Delta T_{max}}{T_{max} \Delta log10(\mathrm{f})}$$

Where ΔT_{max} is the difference among the T_{max} values measured in the $\Delta log_{10}(f)$ frequency range. For weakly or non-interacting superparamagnetic systems, the expected value for the Mydosh parameter Φ must be Φ ~ 0.1–0.13; the values below this interval are characteristic of nanoparticle systems with intermediate interactions and the values below the interval are related to strong interparticle interacting systems or result from spin-glass like surface behavior ($\Phi \sim 5 \times 10^{-3} - 5 \times 10^{-2}$) [24–29]. Consequently, the analyzed systems exhibit the aforementioned shift in Tmax with increasing frequency and a Mydosh parameter value characteristic of spin glasses (see **Figure S7A**).

To verify the above, the frequency-dependent values of χ" were fitted to the 3D critical scaling law for spin dynamics, in which the relaxation time diverges at a finite temperature (Tg≠ 0K), following the equation below:

$$\tau = \tau_0 \left[\frac{T_g}{T_g/T_{max} - T_g} \right]^{zv}$$

Where T_g is the critical temperature of the glassy state, τ_0 the relaxation time, and zv the critical exponent. The values of τ_0 calculated by fitting (see **Figures S7A, S7B, and S7C**) fall within the range of canonical spin glasses (from 10^{-7} to 10^{-12} s), and the value of zv for this same type of system ranges from 4 to 12 [30,31].

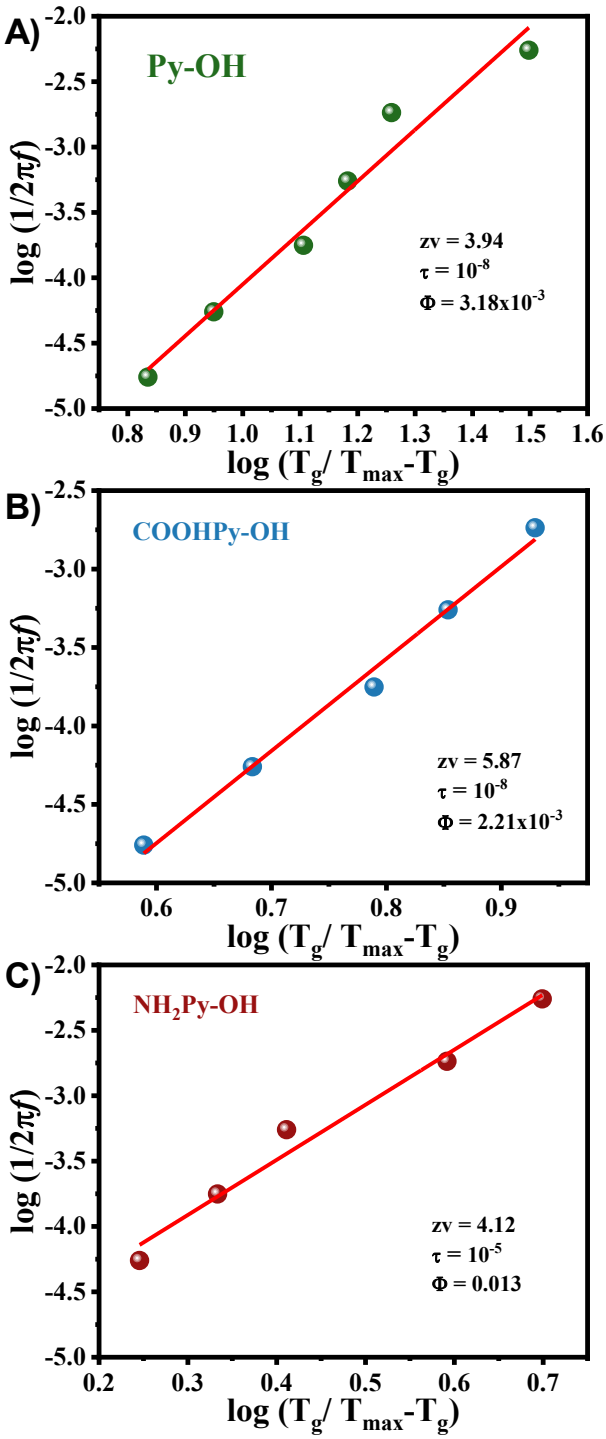

Figure S7. The zv, τ, and Φ values fit closely into a canonical spin glass behavior evident at low temperatures for all samples**.**

References.

1 E. A. Quintanilla-Serrano, P. Acevedo-Peña, J. Vazquez-Samperio, S. Cruz-Orellana, J. Rodríguez-Hernández and E. Reguera, *Electrochim. Acta*, DOI:10.1016/j.electacta.2024.145571.

2 H. Jia, Y. Yao, J. Zhao, Y. Gao, Z. Luo and P. Du, *J. Mater. Chem. A Mater.*, 2018, **6**, 1188–1195.

3 X. Sun, L. Yang, D. Li and Z. Tian, *J. Mol. Struct.*, DOI:10.1016/j.molstruc.2024.140549.

4 J. Liu, W. Li, S. Song, H. Cui, W. Lu, T. Du, X. Zhang and F. Yang, *Int. J. Hydrogen Energy*, 2024, **93**, 374–386.

5 Y. Liao, Y. Xiao, Z. Li, X. Zhou, J. Liu, F. Guo, J. Li and Y. Li, *Small*, DOI:10.1002/smll.202307685.

6 Y. Hao, Q. Liu, Y. Zhou, Z. Yuan, Y. Fan, Z. Ke, C. Y. Su and G. Li, *Energy and Environmental Materials*, 2019, **2**, 18–21.

7 V. Singh, D. K. Singh, M. Yadav, S. Singh, V. Rathour, A. Tiwari and V. Ganesan, *Energy Advances*, 2024, **3**, 636–647.

8 Y. Liu, C. Wang, S. Ju, M. Li, A. Yuan and G. Zhu, *Progress in Natural Science: Materials International*, 2020, **30**, 185–191.

9 Y. Wang, Y. Pan, L. Zhu, H. Yu, B. Duan, R. Wang, Z. Zhang and S. Qiu, *Carbon N. Y.*, 2019, **146**, 671–679.

10 S. Govindaraju, S. K. Arumugasamy, G. Chellasamy and K. Yun, *J. Hazard. Mater.*, DOI:10.1016/j.jhazmat.2021.126720.

11 Y. Fang, X. Li, F. Li, X. Lin, M. Tian, X. Long, X. An, Y. Fu, J. Jin and J. Ma, *J. Power Sources*, 2016, **326**, 50–59.

12 F. F. Wang, P. J. Wei, G. Q. Yu and J. G. Liu, *Chemistry - A European Journal*, 2016, **22**, 382–389.

13 Y. Liu, H. Wang, D. Lin, J. Zhao, C. Liu, J. Xie and Y. Cui, *Nano Res.*, 2017, **10**, 1213–1222.

14 Y. Wang, X. Chen, Q. Lin, A. Kong, Q.-G. Zhai, S. Xie and P. Feng, *Nanoscale*, 2017, **9**, 862–868.

15 H. Sun, H. Su, X. Ma, P. Zhang, X. Zhang, X. Dai, J. Gao, C. Chen and S. G. Sun, *Electrochim. Acta*, 2016, **205**, 53–61.

16 C. Lv, B. Li, Y. Ren, G. Zhang, Z. Lu, L. Li, X. Zhang, X. Yang and X. Yu, *Chemical Engineering Journal*, DOI:10.1016/j.cej.2024.153670.

17 X. Zhang, C. Gao, L. Li, X. Yan, N. Zhang and J. Bao, *J. Colloid Interface Sci.*, 2024, **676**, 871–883.

18 Z. Hu, Q. Geng, S. Dong, M. Wang, Y. Song, W. Sun, H. Diao and D. Yuan, *J. Colloid Interface Sci.*, 2024, **671**, 34–45.

19 T. Lan, H. Du, Y. Li, K. Qu, J. Zhao, X. Zhang, Y. Dong, Y. Zhang, X. Zhang and D. Zhang, *J. Alloys Compd.*, DOI:10.1016/j.jallcom.2023.169144.

20 Y. Liu, J. Niu, X. Liu, J. Qu and A. P. O'Mullane, *Mater. Today Chem.*, DOI:10.1016/j.mtchem.2023.101764.

21 H. Wang, S. Su, T. Yu, C. Meng, H. Zhou, W. Zhao, S. Yan, T. Bian and A. Yuan, *Appl. Surf. Sci.*, DOI:10.1016/j.apsusc.2022.153522.

22 S. Q. Deng, Z. Zhuang, C. A. Zhou, H. Zheng, S. R. Zheng, W. Yan and J. Zhang, *J. Colloid Interface Sci.*, 2023, **641**, 265–276.

23 J. A. Mydosh, *Spin Glasses*, CRC Press, 2014.

24 S. H. Masunaga, R. F. Jardim, P. F. P. Fichtner and J. Rivas, *Phys. Rev. B*, 2009, **80**, 184428.

25 C. Vázquez-Vázquez, M. A. López-Quintela, M. C. Buján-Núñez and J. Rivas, *Journal of Nanoparticle Research*, 2011, **13**, 1663–1676.

26 V. V. Zhakhovskii and S. I. Anisimov, *Journal of Experimental and Theoretical Physics*, 1997, **84**, 734–745.

27 K. Nadeem, H. Krenn, T. Traussnig, R. Würschum, D. V. Szabó and I. Letofsky-Papst, *J. Magn. Magn. Mater.*, 2011, **323**, 1998–2004.

28 O. Moscoso-Londoño, P. Tancredi, D. Muraca, P. Mendoza Zélis, D. Coral, M. B. Fernández van Raap, U. Wolff, V. Neu, C. Damm, C. L. P. de Oliveira, K. R. Pirota, M. Knobel and L. M. Socolovsky, *J. Magn. Magn. Mater.*, 2017, **428**, 105–118.

29 G. F. Goya, *IEEE Trans. Magn.*, 2002, **38**, 2610–2612.

30 J. A. Carrasco, G. Abellán and E. Coronado, *J. Mater. Chem. C Mater.*, 2018, **6**, 1187–1198.

31 A. Sharma and G. Oza, *Nanochemistry*, CRC Press, Boca Raton, 2023.